



Robust shape optimization under model uncertainty of an aircraft wing using proper orthogonal decomposition and inductive design exploration method

Gorkem Demir^{1,2} · Recep M. Gorguluarslan¹ · Selin Aradag³

Received: 14 June 2022 / Revised: 2 December 2022 / Accepted: 20 March 2023 / Published online: 5 April 2023
© The Author(s), under exclusive licence to Springer-Verlag GmbH Germany, part of Springer Nature 2023

Abstract

Robust aerodynamic shape optimization of aircraft components is a computationally expensive process due to a high number of parametrized design variables of complex geometry definitions especially when uncertainties are involved. Therefore, reducing the number of design variables and complexity has vital importance to respond over a range of on-design requirements with the need to meet design constraints in the robust optimization process. In this study, the Proper Orthogonal Decomposition (POD) method is incorporated into the Inductive Design Exploration Method (IDEM) for the aerodynamic shape optimization process of an aircraft wing with reduced computational effort. POD data reduction technique is utilized to filter design variables of the wing by extracting the dominant features of the system to reduce the number of design variables in the robust optimization process. POD-based Radial Basis Function (RBF) data estimation surrogate model is also implemented to enrich design alternatives for the optimization framework with a reduced computational cost. Model uncertainties due to the Computational Fluid Dynamics (CFD) turbulence model are introduced to IDEM as epistemic uncertainties using the eigenspace perturbation methodology. The results of the case study show that the proposed IDEM can obtain robust wing designs satisfying the performance goals while accounting for the uncertainties in the top-to-bottom approach.

Keywords Computational fluid dynamics · Proper orthogonal decomposition · Aircraft wing · Uncertainty · Robust Optimization

1 Introduction

There is a significant challenge to obtain better design alternatives with extreme aircraft performance requirements, due to the advancements in the aviation industry. Therefore, aerodynamic shape optimization especially for the main

components of an aircraft is a primary topic of interest to respond over a range of on-design requirements with the need to meet the design constraints. Most design problems are defined as multi-point and multi-objective optimization formulations where both on and off-design conditions are required as design points. This situation causes the optimization procedure to become a hampered process, and in recent years, efficient optimization techniques are developed to reduce computational cost (Castonguay and Nadarajah 2007; Li and Zhang 2021).

The mathematical definition and parametrization of geometry have a significant impact on engineering design problems. Various geometry alternatives can effortlessly be obtained by changing the parametrized design variables. However, most of the geometries utilized in aerodynamic design consist of complicated curves and surfaces. Thus, geometric definitions cannot be finalized by simple mathematical descriptions. Geometry parametrization techniques can be classified into two main categories in aerospace engineering applications (Sripawadkul et al. 2010). These are computer-aided and analytical-based

Responsible Editor: Seonho Cho

Gorkem Demir, Recep M. Gorguluarslan, and Selin Aradag have contributed equally to this work.

✉ Recep M. Gorguluarslan
recepga@gmail.com

¹ Department of Mechanical Engineering, TOBB University of Economics and Technology, Cankaya, 06560 Ankara, Turkey

² Turkish Aerospace, Kahramankazan, 06980 Ankara, Turkey

³ Department of Mechanical Engineering, TED University, Kolej, 06420 Ankara, Turkey

methods. Complicated geometries can be generated by the Non-Uniform Rational B-spline (NURBS) in modern Computer-Aided Design (CAD) systems; however, design variables for defining curves and surfaces lead to increased computational costs. Similarly, analytical-based methods have a handicap due to difficulties associated with complex geometry definitions. Therefore, reducing the number of design variables and complexity due to computational cost is important for the parametrization of the geometry. In accordance with Sripawadkul et al. (2010), the main parametrization techniques used in the aerodynamic design, which are Ferguson curves (Ferguson 1964), Hicks–Henne bump functions (Hicks and Henne 1978), PARSEC (Farin 1993; Sobieczky 1998), B-Splines (Sobieczky 1998), and Class/Shape functions (Kulfan and Bussoletti 2006), are distinctly explained and scored in terms of parsimony, completeness, flawlessness, intuitiveness, and orthogonality. In this study, it is accepted that B-splines curves are suitable for wing geometry construction. Specifically, Bezier curves that constitute the fundamentals of B-splines are used due to their simplicity.

In the aerodynamic design problems using parameterized geometries, design optimization algorithms have an essential role in quickly reaching the optimized solutions. Both gradient-based and gradient-free optimization methods have been widely used for aerodynamic shape optimization. Gradient-based methods require gradient evaluation or the sensitivity of design variables with respect to objective functions (Yang and Chen 2021). Adjoint-based gradient optimization methods have been developed to provide an efficient way to evaluate the gradients with a computational cost that is independent of the number of design variables (Yu et al. 2018). However, gradient-based optimization methods can face the risk of trapping into the local minimum and do not guarantee the global minimum achievement when the objective or constraint functions involved are highly nonlinear (Bons et al. 2017; Dumont and Meheut 2016; Koo and Zingg 2018; Bird et al. 2021). The gradient-free optimization methods such as the design exploration method (DEM) are a tool frequently used by researchers to better enable optimized design selection (Du et al. 2021; Ye et al. 2021; Amrit et al. 2018). Aerodynamic DEM is generally straightforward to implement and geared toward finding global optima. On the other hand, aerodynamic DEM has significant computational challenges due to requiring large amounts of time and computer resources (Amrit et al. 2018). There is still a crucial bottleneck in terms of the excessive number of required design variables although the most effective geometry parameterization technique is selected for DEM. Therefore, it is essential to reduce the complexity of the problem to overcome this obstacle when DEM is used for design optimization. For this purpose, sensitivity analysis is employed to explore which input parameters have the most influence on the output. However, sensitivity analysis

also has an extensive computational cost for a high number of design variables. To overcome this computational issue due to the high number of design variables in both DEM and sensitivity analysis, dimension reduction techniques can be used. Among various techniques, Proper Orthogonal Decomposition (POD) is preferred in this study for two reasons: First, the POD is a statistical technique that reduces the high dimensional or complex systems to low-dimensional systems by reflecting the dominant characteristic of the system, and its efficacy in the field of aerodynamics is shown in the literature (Zhu et al. 2020; Nagarajan et al. 2009; Lim et al. 2020; Zhou et al. 2020; Cai and Ladeinde 2005; Iuliano and Quagliarella 2013). Second, unlike the existing use of the POD in the literature, in this study, the POD is applied for geometric filtering by extracting dominant characteristics of wing design parameters. Thus, as a contribution of this study to the literature, it is shown that the wing geometries required for the design space exploration can be reconstructed with parametrization of the POD basis rather than using the basis function of the Bezier surface method.

The sampling of design space through the Design and Analysis of Computer Experiments (DACE) is a substantial procedure to train surrogate models to establish a correlation between the design variables and quantities of interest (Kennard and Stone 1969; Raul and Leifsson 2021). Evaluation of true response quantities is another important issue in terms of computational cost (Iuliano 2017). The decision on the DACE strategy has paramount importance on the accuracy of the surrogate model. In common usage, random sampling methods are suitable for capturing all portions of the design space when the trend of the response surface is unknown. Classical DACE methods lead to an intensive sampling of the design space for a nonlinear and larger dimension of the exploration space (Huntington and Lyrantzis 1998). Therefore, Latin Hypercube Sampling (LHS) which is a classical sampling method is preferred as the DACE technique.

POD is a favorable technique to reflect a low-order and qualified approximation of a system. POD has no prediction capability of unknown design points to enrich design space (Iuliano 2011). Therefore, a data fitting technique is intimately implemented to establish a functional relationship between the dominant characteristic of the system and responses. POD has widely been used for linear regression models; however, reasonable results cannot be obtained using POD when nonlinear behavior is dominant. The main reason behind this is that the linear regression models cannot extract the nonlinear behavior (Xin et al. 2015). In this study, to overcome this situation, a nonlinear regression method called radial basis function (RBF), which is highly preferred for scattered observations, is utilized for determining POD coefficients (Rogers et al. 2012; Benaissa et al. 2017). By taking the interpolation ability advantage of RBF, POD has become a predictive method to retrieve the approximation of unknown points.

In aerodynamic design studies, uncertainty estimation is one of the most challenging concerns in the optimization process and has a significant impact on design conditions. Uncertainties can mainly be divided into two categories: aleatory and epistemic uncertainty (Caboni et al. 2018). Aleatory uncertainties are associated with natural randomness; in other words, the probability of input variations of a system. Epistemic uncertainties are related to limited information in the model of the process, for instance, uncertainties arising due to turbulence models used in the Reynolds-averaged Navier–Stokes (RANS) models in Computational Fluid Dynamics (CFD) analyses. In this study, an epistemic model-form uncertainty estimation technique due to turbulence closure problem in the RANS models is considered by perturbing the Reynold stress projections within the physically realizable limiting states called the Eigenspace Perturbation Methodology (Mishra et al. 2018; Emory et al. 2011; Xiao et al. 2016).

Robust optimization is a design methodology for a system taking uncertainties into account (Du et al. 2021; Zhang et al. 2021; Fusi and Quaranta 2020). There are three robust solution categories describing the performance obtained by minimizing variations of different elements of the solution space (Choi et al. 2005). (i) One category includes the minimization of the variation that cannot be controlled by the designer, (ii) the second one is related to the minimization of the control factors that can be controlled by the designer, and (iii) the last strategy is to minimize the deviation due to the uncertainty inherent of the model (Choi et al. 2008). The robust optimization approach called Inductive Design Exploration Method (IDEM) proposed by Choi et al. (2005), Bird et al. (2021), Jang et al. (2018) is a recursive process that links multiple design levels to determine the combinations of input parameters that provide robust solutions to the ranged set of requirements specified for top-level performance parameters. The computational burden of the existing method, on the other hand, is an important issue when the number of design variables is high. Choi et al. (2005) state that the traditional IDEM has a high computational expense when used for complex problems. The existing studies that utilize IDEM (Choi et al. 2005, 2008; Jang et al. 2018) used two to five design variables in the presented problems which are very small numbers. Efficient solutions are needed to enable the use of IDEM for complex problems such as the shape optimization problems in the aerospace industry because those problems involve a high number of design variables, model uncertainties, multiple objectives, and expensive CFD simulations which make the solution of the problems prohibitive.

To overcome this issue, our main contributions are twofold: (1) Inductive Design Exploration Method (IDEM) is introduced to the aerodynamic field for the first time to find the optimal design range for a multi-objective shape optimization

problem. (2) To overcome the computational intensity of the IDEM, the POD approach is adopted for design variable reduction, and the POD-based RBF surrogate model is implemented for the accurate prediction of the computationally expensive CFD simulation results. Thus, the novelty of this research is to show that the IDEM integrated with the POD and RBF is an effective approach for solving an aerodynamic design optimization problem with high complexity under model uncertainties.

The paper is organized as follows: In Sect. 2, the methodology used for the robust optimization of the aircraft wing is described with relevant methods and formulations. In Sect. 3, the application of the presented methodology for the aircraft wing design is demonstrated and the results are discussed. The conclusions are given in Sect. 4.

2 Methodology

2.1 Geometry parametrization

Geometry parametrization is an important procedure for manipulating any geometry effortlessly. Bezier curves are parametric approximating curves that provide the mathematical description of a geometrical shape (Kumar et al. 2012). An n -th order Bezier curve can be expressed as follows:

$$z(t) = \sum_{i=0}^n B_i^n(t) P_i, \quad (1)$$

where n is the degree of Bezier curves, $B_i^n(t)$ are the Bernstein polynomials, P_i are the $n + 1$ control points, and t is the curvilinear coordinates. Bezier surfaces can fundamentally be defined as the extension of Bezier curves. A Bezier curve is defined by a control polygon of the control points whereas a Bezier surface is defined by a control polyhedron of the control points. Therefore, the Bezier surfaces can be expressed as follows:

$$p(u, w) = \sum_{i=0}^m \sum_{j=0}^n P_{ij} B_{i,m}(u) B_{j,n}(w), \quad (2)$$

where P_{ij} are the control vertices of the polyhedron, B is the Bernstein polynomial, u and w are the parameters identifying surface patch in the range of $[0, 1]$. Bernstein polynomials are calculated by

$$B_{i,n}(u) = \frac{n!}{i!(n-i)!} u^i (1-u)^{n-i}. \quad (3)$$

2.2 Proper orthogonal decomposition (POD)

Dominant features that contain as much information as possible of a system are extracted from a given set of data using

the POD technique. The snapshot matrix (S_j) (Sirovich 1997) is constructed using the given data set that can be pressure, drag coefficient, pressure sound level, etc.

$$S_j = [S_1, S_2, \dots, S_M] \quad \text{for } j = 1, 2, \dots, M, \quad (4)$$

where M is the total number of parameters. The deviation of each element in the snapshot matrix is calculated by subtracting the mean of the snapshot matrix elements from each element (Newman 1996; Deane et al. 1991). Thus, the deviation matrix is given by

$$V_j = \left[S_1 - \frac{1}{M} \sum_{j=1}^M S_j, S_2 - \frac{1}{M} \sum_{j=1}^M S_j, \dots, S_M - \frac{1}{M} \sum_{j=1}^M S_j \right]. \quad (5)$$

Basis functions (φ_j), which are the set of optimum linear equations consisting of the most energetic characteristic of a snapshot matrix, are derived to reflect the exact behavior of the system using POD.

$$\varphi_j = \sum_{j=1}^M \alpha_j V_j. \quad (6)$$

In Eq. (6), α_j are described as the relative mode amplitudes. The procedure is followed by computing the correlation matrix (R_{ij}) that is defined as the integral of the inner product of the deviation at different points of the snapshot matrix.

$$R_{ij} = \frac{1}{M} \int_{\Omega} V_i(x) V_j(x) dx \quad i, j = 1, 2, \dots, M \quad (7)$$

The correlation matrix is a non-negative matrix that includes eigenvalues and orthogonal eigenvectors. The Singular Value Decomposition (SVD) method is used to obtain the eigenvalues and eigenvectors of a correlation matrix given by

$$[R] = [C] \left[\sum \right] [P]^T, \quad (8)$$

where $[C]$ is the orthogonal eigenvector matrix, in which the POD coefficients or modes are in the first column of the matrix, $[\sum]$ represents the non-negative diagonal matrix containing the eigenvalues $\sigma_1, \sigma_2, \dots, \sigma_M$, and $[P]$ denotes the right eigenvector. Dominant modes of the system are put in an order from the higher energy content to lower energy content. The total energy content of the POD coefficients controls the primary information of the system. To reduce the degree of freedom of the system by using the POD method, the energy level of the system (E_p), which should be greater than an energy threshold (ϵ) decided by the user, is expressed as follows:

$$E_p = \frac{\sum_{i=1}^N \sigma_i}{\sum_{j=1}^M \sigma_j} \geq \epsilon, \quad (9)$$

where N denotes the number of selected eigenvalues such that $N \leq M$. The energy level is commonly set as 99% total energy of system (Iuliano and Quagliarella 2013). Once the number of eigenvalues N that satisfies Eq. (9) is determined, the snapshot matrix can be reconstructed using the basis functions with the reduced number of design variables by

$$[\tilde{S}] = [\bar{S}] + \sum_{i=1}^N \alpha_i \varphi_i \text{ or } [\tilde{S}] = [\bar{S}] + [\varphi][\alpha], \quad (10)$$

where \bar{S} denotes the mean value of the snapshot matrix, $[\alpha]$ denotes the amplitude matrix that includes α_i .

2.3 POD-RBF surrogate modeling technique

POD is not capable of estimating the response of an unknown point available in the design space. Therefore, a data fitting technique is implemented to establish a functional relation to explore the design space. In this study, the RBF method is utilized to be the interpolating function with the data fitting in the POD to estimate the response (Xin et al. 2015). Let $[x]$ be the observation vector with n number of observations, then the RBF approximation of the j th observation denoted by $s(x_j)$ is expressed as follows:

$$s(x_j) = \sum_{i=1}^n n(w_i \theta \|x_j - x_i\|), \quad (11)$$

where $r = \|x_j - x_i\|$ denotes the Euclidean norm calculated for an observation x_j with respect to each observation x_i in $[x]$, w_i are the weights or coefficients of the estimation and θ is the radial basis function. The multiquadric function is used in this study due to its simplicity and good accuracy compared to the various RBFs such as the cubic, thin plate spline, and Gaussian functions (Xin et al. 2015; Kutkan 2018). The multiquadric function is given by

$$\theta(r) = \sqrt{r^2 + c^2}, \quad (12)$$

where c is a smoothing factor and r is the Euclidean norm. Wendland's functions (Wendland 1995) are also other types of RBFs that have the potential to bring better prediction accuracy than the other RBF methods (Fornet et al. 2001; Romani et al. 2019). Wendland's functions were out of the scope of this work but should be considered in future studies. To use the RBF in POD, the amplitude matrix $[\alpha]$ can be written as follows (Rogers et al. 2012; Benaissa et al. 2017):

$$[\alpha] = [B][F], \quad (13)$$

where $[B]$ denotes the coefficient matrix to be computed, and $[F]$ is the interpolation matrix. In Eq. (13), $[\alpha]$, $[B]$, and $[F]$ respectively represent $s(x_j)$, w_i , and $\theta\|x_j - x_i\|$ in the RBF defined by Eq. (11). If both sides are multiplied by $[F]^{-1}$ then Eq. (13) is written as follows:

$$[B] = [\alpha][F]^{-1}. \quad (14)$$

The basis functions can be written as follows:

$$[\hat{\phi}]^T[V] = [B][F]. \quad (15)$$

The snapshot matrix can be estimated as follows:

$$[\tilde{S}] = [\tilde{S}] + [\hat{\phi}][B][F]. \quad (16)$$

POD approach can be used as a predictive feature by utilizing the RBF functions. In this study, estimation of design points available in the design space is performed by using this POD-RBF surrogate model.

2.4 Model-form uncertainty using eigenspace perturbation methodology

Uncertainties can exist due to two main reasons (Caboni et al. 2018). The first one is the uncertainties introduced to the input parameters by manufacturing, material, etc. The second one is called the model-form uncertainty which is introduced due to the uncertainties of the computational model used for simulations. In this study, the second uncertainty type is taken into account since it plays a more significant role due to RANS-based modeling than the first type (Mishra et al. 2018; Emory et al. 2011; Xiao et al. 2016). Specifically, there are deviations or uncertainties observed in the results acquired from CFD analyses of aircraft components due to the turbulence closure problem in the RANS simulations. The model-form uncertainty originating from the shear stress transport (SST) k - ω turbulence model is determined using the eigenspace perturbation methodology (Mishra et al. 2018; Emory et al. 2011; Xiao et al. 2016). The eigenspace perturbation process is shown in Fig. S1, and the details of this methodology with its formulations are explained in Supplementary document-S1.

In this study, the flowchart of the eigenspace perturbation methodology to include the model-form uncertainty is depicted in Fig. 1. To implement this methodology, first, the simulation conditions such as the boundary, initial conditions, flux splitting method, etc. are defined. The

unperturbed Reynolds stress tensor for each node of the computational grid is calculated based on these simulation conditions. Then, the eigenspace perturbation is utilized and the perturbed Reynolds stress tensor required for turbulent and convective flux computations is calculated. The new perturbed fluxes are then used to march the solution forward in pseudo-time. As the solution converges, the Reynolds stress tensor also converges to its perturbed state. The five distinct simulations are performed using this method in Fig. 1 and the uncertainty bounds are determined with respect to the unperturbed state.

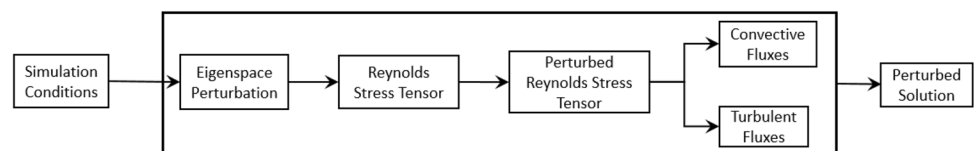
2.5 Inductive design exploration method (IDEM)

Inductive Design Exploration Method (IDEM) (Choi et al. 2005) is a top-down robust optimization process that allows determining the feasible input parameters according to a set of performance requirements including noise and control factors, and model uncertainty. The main idea is to find an optimal design space based on Hyper-Dimensional Error Margin Index (HD-EMI) by preventing cumulative uncertainty due to model and input parameters. In this study, HD-EMI value calculations are only based on the model uncertainties. The IDEM procedure is summarized with the following steps:

- The design space in correspondence with input parameters is defined.
- The output parameters are evaluated using mapping and/or simulation models to generate the output space. The input and output spaces are stored as a database.
- Performance and constraint requirements are described. The boundary of the initial design requirements is determined by using Delaunay Triangulation (convex hull) (Kern et al. 2017). Thus, the relation between the feasible region and design space is established.
- HD-EMI value considering model uncertainties is computed for each output parameter and design alternatives.
- Feasible designs, the HD-EMI value of which are higher than the specified HD-EMI threshold, are selected.

HD-EMI is a feasible space selection criterion considering uncertainties to observe that the response of each design alternative satisfies the performance requirements. HD-EMI threshold is defined to assess whether candidate solutions are accepted or rejected. If the mean of an output range is

Fig. 1 The flowchart of the uncertainty quantification process



in the feasible ranges, the HD-EMI value is positive. When the mean of an output range is not in the feasible range, then the HD-EMI value is negative unity, which means the input variable is unsatisfactory for the feasible region in the design space. Its mathematical formulation can be expressed as Kern et al. (2017):

$$HD_{EMI} = \begin{cases} \min_i \frac{\|\bar{y} - B_{j,i}\|}{\Delta y_i} \\ -1 \end{cases}, \quad (17)$$

where i and j represent the output dimension Δy_i denotes the distance between the mean of the output range and the maximum or minimum value of the output range considering uncertainty. $\|\bar{y} - B_{j,i}\|$ is the distance between the boundary $B_{j,i}$ computed by the performance requirements and the mean of the output range denoted by \bar{y} .

2.6 Proposed POD-based IDEM framework

The computational cost of the IDEM procedure increases dramatically when the number of design variables is high since an adequate number of sampling points should be generated and evaluated in the design space for accurate predictions of the optimized solutions. In this study, the POD method is integrated with the IDEM to reduce the input parameter dimension and achieve a surrogate model of the expensive CFD analyses to reduce the computational cost. The proposed IDEM framework can be explained by the following steps:

- The priori design space filling is performed using the actual number of the design variables (M). At least $15 \times M$ design alternatives are required to be generated in total (Afzal et al. 2017) to build the design space used in the POD model defined in Sect. 2.2. It should be noted that the CFD analyses are not required to generate the design variable values for the design alternatives. However, the CFD analysis will be required to evaluate the performance of each design alternative in the design space. In this study, the design alternatives are generated using the design variables explained in Sect. 2.1. Specifically, the coordinates of the control points are considered as the design variables.
- In the POD method, the snapshot matrix defined in Sect. 2.2 is constructed using the initial database. The dominant POD coefficients which satisfy 99% total energy of the snapshot matrix are extracted to identify the geometry.
- The geometry database is reconstructed by using the N number of POD coefficients instead of the actual number of design variables. New design space filling by the LHS method is employed with $15 \times N$ and the true responses of the design points are evaluated with the CFD analyses.

- The POD-RBF surrogate model described in Sect. 2.3 is trained with the ensemble data which is obtained by the CFD analysis results.
- The design space is enriched with the discrete points evaluated by LHS and the response of the design points is estimated by POD-RBF.
- The input space is arranged with the POD coefficients and the output space is defined with the true and estimated responses of the input space.
- Performance requirements are identified and the feasible region available in the output space is determined.
- Model uncertainty values determined by the method explained in Sect. 2.4 are identified for each output parameter.
- HD-EMI threshold is set as 1 (Choi et al. 2008) to determine the robustness level of each design alternatives.
- Robust solutions are obtained and listed in accordance with the HD-EMI and objective function values using IDEM described in Sect. 2.5.

3 Results and discussion

3.1 Problem definition of the aircraft wing design optimization

In this study, an aircraft wing design optimization problem is solved by using the proposed POD-based IDEM framework. It is necessary to define the problem before describing the implementation details of the proposed method. There are three design objectives that are aimed to be improved in the design optimization of the wing problem:

1. Rolling moment coefficient gradient ($CR - \beta$),
2. Lift coefficient (CL),
3. Drag coefficient (CD).

The three different cases of flow conditions listed in Table 1 were considered based on the information given by the literature (Yildirim 2021). Further details of these three cases are described as follows:

- Case 1: The design objective $CR - \beta$ is intended to be minimized to satisfy the approach scenario of an aircraft extracting flap configuration at sea-level altitude (Yildirim 2021). The flow conditions for Case 1 are mentioned: Mach number is 0.18, the angle of attack (AOA) is 8° , and the side-slip angle (β) is 10° at the sea level (Yildirim 2021).
- Case 2: The purpose of Case 2 is to improve the loop-maneuvering entrance at 3048 m (10,000 ft) pressure altitude. Since it is known that the increase of CL will directly improve the loop-maneuvering entrance (Yildirim 2021), the design

Table 1 Design objectives and flow conditions

Case number	Design objective	Flow conditions			
		Mach number	Angle of attack (AOA)	Side-slip angle	Pressure altitude
Case 1	Minimize $CR - \beta$	0.18	8	10	Sea level
Case 2	Maximize CL	0.4	10	0	3048 m (10,000 ft)
Case 3	Minimize CD/CL	0.53	-1	0	Sea level

objective CL is aimed to be maximized in this case. The flow conditions for Case 2 are mentioned: Mach number is 0.4, AOA is 10° , and β is 0° . These flow conditions are considered for the case without the side wind condition (Yildirim 2021).

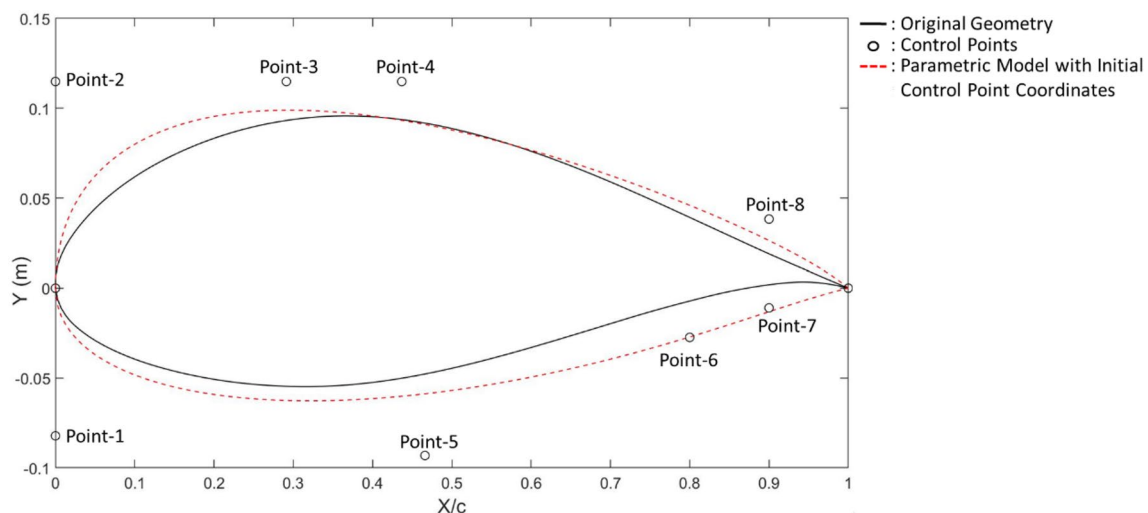
- Case 3: The design objective CD is aimed to be minimized while the CL is aimed to be maximized to improve the high-speed characteristic of the aircraft at sea-level altitude (Anderson 1999). Since there are two objectives and the maximization of CL can be formulated as minimization of its inverse (i.e., $1/CL$), the ratio CD/CL is defined to be minimized. The flow conditions are mentioned: Mach number is 0.53, AOA is 0° and β is 0° at the sea level. Mach number without side wind condition is selected in accordance with Yildirim (2021) and the details of the calculations of the flow conditions are given in Supplementary Material-S2.

3.2 Geometry parametrization

The aircraft wing geometry was generated using two airfoil sections that are root and tip. The airfoil geometries were parameterized using parametric Bezier curves described in Sect. 2.1. The goal of parameterization was to enable the

change of the wing geometry during the robust optimization process based on the geometric parameters, which were defined to be the control points of the Bezier curves. The wing geometry was defined by two airfoils at two ends of the wing. Each of these two airfoil geometries was divided into two sections as upper and lower curves described in Amrit et al. (2018), Ren et al. (2016). Parametrization of each upper and lower sections of airfoil profiles was performed using 5th-degree Bezier curves because in the existing literature (Amrit et al. 2018) 5th-degree Bezier curves were shown to be suitable to model the airfoils. The leading and trailing edge points were the common points of the upper and lower sections and were modeled as constant for the airfoil parametrization as shown in Fig. 2. The remaining control points in between these fixed leading and trailing edge points (points 1–8 shown in Fig. 2) can move in the x - and y -directions. Among those, points 1 and 2 on the left-hand side in Fig. 2, were aligned to have the same initial x -coordinate value to capture the leading edge radius. The initial coordinates of the other control points were unequally spaced as suggested by Amrit et al. (2018) and Fusi and Quaranta (2020).

It should be noted that in the airfoil-fitting process, it is sufficient to vary only the middle control points (i.e., points 1–8). The start and end control points, i.e., the leading and

**Fig. 2** Airfoil shape parametrization using Bezier curves

trailing edge control points are fixed for the airfoil-fitting process. On the other hand, for the entire 3D wing geometry used in the shape optimization, the locations of the leading and trailing edge control points change with the other wing geometry parameters which are the taper and aspect ratios, twist, dihedral, and sweep angles. That means, four Bezier control points are required to model each curve of the airfoil sections. Then, to generate the 3D wing geometry using the two end airfoils, 16 control points as the middle control points are required as the independent parameters. Each of these control points has two design variables which are the X and Z coordinates. Thus, a total of 32 coordinate values are required as the design variables to model airfoil sections.

After generating the two end airfoils of the wing, the wing surfaces are modeled between the two ends with the upper and lower surfaces.

In addition to the Bezier control points that define the airfoil shapes of the wing, five additional design variables are defined to construct the wing geometry. These additional variables determine the Z coordinates of the Bezier control points as well as the positions of the coordinates of the leading and trailing edge control points with respect to each other. These five additional design variables are the taper and aspect ratio, dihedral, sweep, and twist angle. These

details of these design variables are explained in Supplementary Material S3 and shown in Fig. S3. As a result of the parametrization process, 37 design variables are required to define the wing geometry. The initial root and tip airfoils were selected as NACA 63415 laminar type airfoil and three-dimensional wing parameter values are listed in Table 2.

3.3 Reduction of design variables by POD

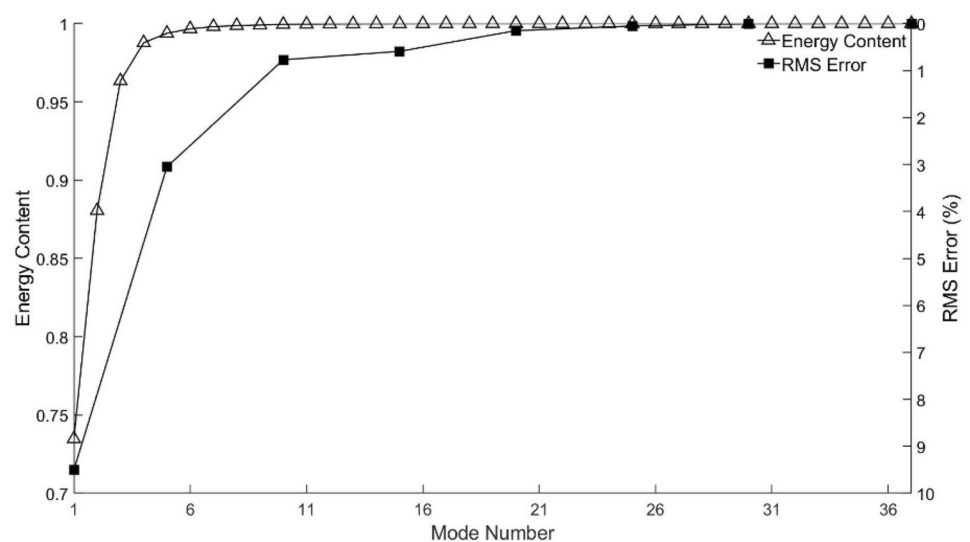
The computational effort of the design exploration process dramatically increases with the increase of the number of design variables. The POD approach described in Sect. 2.2 was utilized in this study to reduce the number of design variables by extracting the dominant behavior of the problem. The number of original design variables was set as $M = 37$ and a priori LHS was employed to initialize the design space population in accordance with the upper and lower design limits in Table 2 for the snapshot matrix. Eigenvalues of the design space were extracted and listed in decreasing order of the importance using SVD by Eq. (8). Dominant modes of the system were selected to compensate 99% energy content of the system by Eq. (9). Along with the energy contents, the root-mean-square (RMS) errors between the reconstructed geometry with the reduced-order model and the original geometry (with a total number of 37 eigenvalues) were calculated and shown in Fig. 3 for comparison to evaluate the influence of the number of modes on the representation of the given dataset.

It is apparent from Fig. 3 that the first 5 modes of the system are sufficient to define the geometry with high accuracy according to the energy content (i.e., <99%). However, the RMS error curve converges after 25 modes. Hence, 25 modes are accepted as the adequate dominant modes to obtain different geometry alternatives according to the RMS

Table 2 Upper and lower limits of wing design parameters

Parameter	Initial values	Lower limit	Upper limit
Wing area (m ²)	16.2	16.2	16.2
Aspect ratio	5.75	4.5	7.5
Taper ratio	0.45	0.35	0.75
Sweep angle (°)	5	4	12
Dihedral angle (°)	5	2	8
Twist angle (°)	− 1.5	0	− 4

Fig. 3 The energy content and RMS error results with the change of the number of modes



error results. On the other hand, when 25 modes are used, although the number of design variables can be reduced from 37 to 25, the problem still has a high number of design variables.

To further evaluate the differences, two optimization processes were conducted in this study, one with 5 modes and the other one with 25 modes. This means that the dominant POD coefficients were used to parametrize the wing geometry to obtain different wing alternatives. The number of design variables in the optimization was reduced from 37 to 25 and 5. Thus, POD coefficients became the new design variables. Within the shape optimization framework, the LHS was applied to the POD coefficients to obtain the alternative samples of the geometry. The bounds of the POD coefficients used in the LHS method are listed in Tables 10 and 11, respectively.

3.4 Response surface modeling by POD-RBF

The POD-RBF surrogate modeling technique described in Sect. 2.3 is utilized in this study to predict the CFD analysis results within the bounds of interest given in Table 2. For this purpose, a design space-filling process (LHS) is employed to generate samples within the design space for which the CFD analysis is carried out to obtain the training data of the surrogate model. The surrogate model is constructed for the reduced-order models obtained by using the POD study applied in Sect. 3.3. Hence, the samples are generated for the reduced design variables, i.e., the POD modes, and the corresponding modified wing geometries are constructed. Then the CFD analysis is carried out for the wing geometry corresponding to each sample point generated by LHS. The CFD analyses are performed using a reliable open-source solver SU2 which is based on the Finite Volume methodology (Economou et al. 2015). Steady-state simulations are performed for Reynolds numbers of 8.9 million, 21.1 million, and 24.6 million for the computational cases given in Table 1 (Case 1, Case 2, and Case 3), respectively. There are various convective flux discretization schemes which are Jameson–Schmidt–Tuker (JST), Roe, AUSM, HLLC, and Roe–Tuker available as a numerical solution scheme available in SU2 software (Economou et al. 2015). In this study, the JST convective flux splitting method with matrix dissipation, which is suitable for steady-state computations for a wide flow regime, is selected (Jameson 1994; Wen-long et al. 2011). The classical dissipation term is scaled by the flux Jacobian with the minimum eigenvalue. SST $k-\omega$ turbulence model which is accurate for the separation prediction caused by the inverse pressure gradient and combines the advantages of the standard $k-\epsilon$ and standard $k-\omega$ turbulence models is used in the CFD analyses (Menter 1994). Pressure far-field boundary condition, for which Riemann invariants are used to determine the flow variables, is

specified to model the free-stream condition (Schulze 2005). Wing surfaces are modeled with no-slip wall boundary conditions. The flow solver convergence criterion is the one that occurs first of the two conditions: the change in the $CR - \beta$ for Case 1, CL for Case 2, CL and CD for Case 3 value over the last 100 iterations or a maximum number of iterations of 3500 is met. The details of the CFD analyses and grid independency study are given in Supplementary Material-S4.

The smoothing factor denoted by c in Eq. (12) was an important parameter that influences the accuracy of the POD-RBF surrogate model. In this study, a cross-validation methodology was employed to seek the optimal smoothing factor. For this purpose, randomly selected 20% of the sample data was used for validation of the trained surrogate model to be generalized for not new data. Inferior-adjusted R^2 diagnostic metric (Akossou and Palm 2013) was calculated between the results of the CFD analyses and surrogate model estimations for all design objectives for various smoothing factors between 0 and 8000. The number of modes was selected to be 30 and constant for both design spaces to compensate 99% of total energy content for the surrogate model.

For both design variable cases of 5 and 25 POD coefficients, the results converged after about $c = 6500$. Therefore, the smoothing factor was set as 6500 for the POD-RBF surrogate model. For a constant smoothing factor value of 6500, adjusted R^2 results were also calculated by varying the number of modes between 1 and 70 to comparatively show that selecting 30 modes for the POD-RBF modeling was appropriate. For the case of 5 design variables, the adjusted R^2 value reached one after almost three dominant modes and quantitatively has 99% of the total energy content of the system after the first 10 dominant modes. For the case of 25 design variables, on the other hand, R^2 values converged after 30 dominant modes, which was also the same number of modes to represent 99% of total energy content and the results were similar for the design space with 25 POD coefficients.

An in-house Python script was developed for the POD-RBF surrogate modeling. To verify the performance of the developed code, the adjusted R^2 values obtained for all design objectives by the POD-RBF surrogate model are compared by the surrogate model prediction capability of the open-source software called DAKOTA (Dalbey et al. 2020). The results for the in-house POD-RBF and DAKOTA-RBF with two reduced-order design spaces are listed in Table 2.

The results in Table 2 show that both methods are suitable for the estimation. It is also observed that the in-house developed POD-RBF code gives more accurate results compared to the DAKOTA-RBF algorithm when the input variables are increasing. In the light of these results, it is concluded that POD-RBF is an effective surrogate modeling technique.

Table 3 Comparison of adjusted R^2 with 5 and 25 POD coefficients between POD-RBF and DAKOTA

Method	0.18 M $CR - \beta$	0.4 M CL	0.53 M CL	0.53 M CD
Design space generated with 5 POD modes				
POD-RBF	0.999	0.999	0.997	0.991
Dakota-RBF	0.999	0.999	0.991	0.985
Design space generated with 25 POD modes				
POD-RBF	0.997	0.967	0.980	0.947
Dakota-RBF	0.998	0.945	0.975	0.926

3.5 Introduction of model uncertainty

The eigenspace perturbation methodology described in Sect. 2.4 is implemented in this study. Both eigenvalue and eigenvector perturbations are performed to determine the uncertainty due to the turbulence model. Five distinct CFD analyses are performed to estimate the model uncertainty as explained in Sect. 2.4. The perturbed and unperturbed solutions performed for the initial wing geometry are compared for three design objectives (i.e., $CR - \beta$, CL , CD) for three cases described in Sect. 3.1. The calculated uncertainty bounds are given in Table 3.

For Case 1, it is seen from the first column of Table 5 that the lower bound is calculated to be greater than the unperturbed CFD result. In this case, the lower bound is set to the unperturbed CFD result as it is smaller than the perturbed lower bound value. Hence, the upper and lower bounds of the $CR - \beta$ value for Case 1 are obtained. For Case 2, on the other hand, the lower and upper bounds of CL obtained from the perturbation method were found to be on two sides of the unperturbed result as seen in the second column of Table 5. Hence, these perturbed results are set to be the lower and upper uncertainty bounds for Case 2. For the CL results of Case 3 given in the third column of Table 5, similar behavior of Case 1 exists. That is, the lower bound obtained by the perturbation method is greater than the unperturbed result. Hence, the unperturbed result is set to be the lower bound. For the DC result of Case 3, the behavior is similar to the one for Case 2. Hence, the lower and upper uncertainty bounds of the DC are set to be the bounds determined from the perturbation method.

Among these three cases, most of the uncertainty is observed for Case 3 with a 5.29% difference of CL compared to its upper bound and 12.71% and 10.46% differences of DC compared to its upper and lower bounds. The reason for the higher uncertainties can be attributed to the higher velocity and lower AOA values of Case 3 compared to the

Table 4 Uncertainty limits between the perturbed and unperturbed solutions

Uncertainty limit	$CR - \beta$ @Case-1	CL @Case-2	CL @Case-3	DC @Case-3
Lower bound of perturbed CFD result	− 0.001467	1.045	0.133	91.94
Unperturbed CFD result	− 0.001468	1.048	0.131	102.68
Upper bound of perturbed CFD result	− 0.001461	1.065	0.138	115.73

Table 5 Mathematical form of robust optimization

Design space
POD coefficients as design variables
Response
Optimized POD coefficients constructing robust wing design alternatives
Constraints
$CR - \beta$ @Case − 1 \leq − 0.0004363°
CL @Case − 2 \geq 1.05
CL @Case − 3 \geq 0.1
HD-EMI \geq 1.0
Uncertainty
$CR - \beta$ @Case − 1 (%) = [0, 0.48]
CL @Case − 2 (%) = [0.33, 1.54]
CL @Case − 3 (%) = [0, 5.29]
CD @Case − 3 (%) = [10.46, 12.71]
Minimize
$Z = w_1(F_{CR-\beta@Case-1}^*) + w_2(F_{CL@Case-2}^*) + w_3(F_{CD/CL@Case-3}^*)$
$w_1, w_2 = 0.33, w_3 = 0.34$

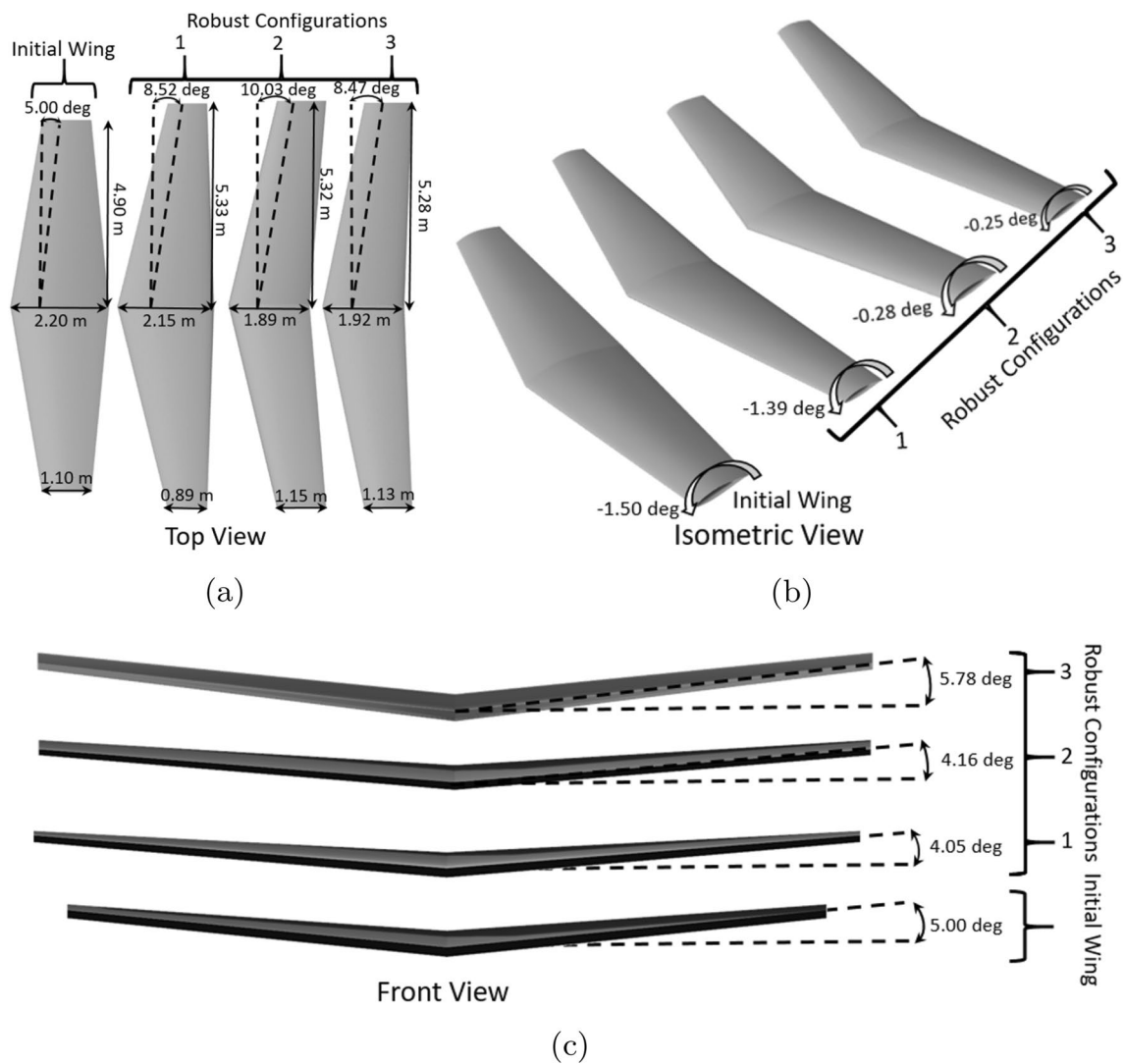
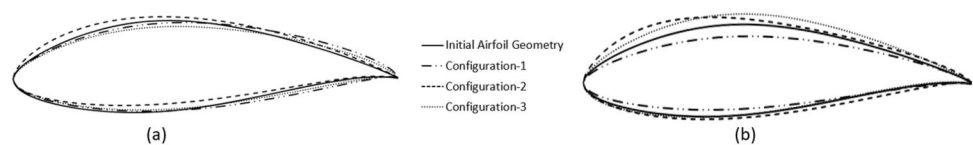


Fig. 4 Robust solutions obtained with minimum objective value by 5 and 25 POD coefficients and 37 design variables **a** Top view, **b** Isometric view, **c** Front view

Fig. 5 Robust airfoil profiles **a** root and **b** tip airfoil profiles for 5 and 25 POD coefficients, and 37 design variables



first two cases. These values lead to more dominant viscous effects for both CL and DC for Case 3, which eventually results in larger bounds for the uncertainty. In this study, uncertainty estimations are implemented for robust optimization computation.

It should be noted that the computational effort required for the uncertainty limit calculations for each design changes dramatically increases because five distinct analyses should be performed to determine the uncertainty limits for each design change. Also, the changes in the uncertainty limits for

each design alternative are assumed to be negligible when considering the additional computational effort required to calculate uncertainty limits for each design change. For these reasons, the changes of the uncertainty limits for different design alternatives were neglected and they were assumed to be the same as the limits for the initial design given by Table 4 to minimize the computational effort. The uncertainty limits for five different design alternatives available in the design space have been calculated and shown

Table 6 Results of three robust design configurations with minimum objective values for 5 and 25 POD coefficients, and 37 design variables

Configuration	Taper ratio	Aspect ratio	Dihedral angle (°)	Sweep angle (°)	Twist angle (°)	Objective function	HD-EMI
Initial	0.50	5.91	5.00	5.00	− 1.50	0.546	0.743
5 POD coefficients	0.41	7.01	4.05	8.52	− 1.39	0.340	1.084
225 POD coefficients	0.61	6.99	4.16	10.03	− 0.28	0.176	1.145
37 Design variables	0.59	6.89	5.78	8.47	− 0.25	0.166	1.229

in Supplementary document-S5 to indicate why the same uncertainty limits can be used.

3.6 Application of IDEM for aircraft wing design

In this study, the open-source python code for IDEM, called pyDEM (Kern et al. 2017) is modified to include the POD-RBF surrogate modeling capability and the model-form uncertainties obtained by the eigenspace perturbation method. To verify the effectiveness of the modified pyDEM code, it is implemented to the wing shape design exploration benchmark case. According to Marler and Arora (2004), 4123 discrete design points are used for the IDEM robust optimization process. To have a similar design point number, in this study, 5000 additional design points are generated to be available in the design space given in Tables 10 and 11, respectively which are different from the training data derived using LHS. The responses of the design points are evaluated by the POD-RBF data prediction algorithm. The robust solutions are searched from the design points by IDEM.

3.6.1 Wing shape design exploration benchmark case

In this section, the proposed IDEM is applied to two different design spaces constructed using 5 and 25 POD coefficients for the wing shape design exploration problem. Since there are three design objectives from three cases with different flow conditions given in Table 1, the shape optimization of the wing is a multi-objective optimization problem. In this optimization problem, a typical performance objective is to minimize $CR - \beta$ and CD/CL for Case 1 and Case 3, respectively, and maximize CL for Case 2. The maximization objective of CL can be identified to the optimization as the minimization of $1/CL$. Since there are multiple objectives to be minimized simultaneously, for the sake of proper objective function minimization, the objective functions are normalized to the same order to eliminate the errors due to the different scales of the objective functions (Rao and Roy 1988). The normalization process of the i -th objective function is given as follows:

$$F_i^* = \frac{F_i(x) - F_i^{\min}}{F_i^{\max} - F_i^{\min}}, \quad (18)$$

where F_i^* denotes the normalized objective function, $F_i(x)$ is the original objective function, F_i^{\max} and F_i^{\min} are the maximum and minimum response available in the design space, respectively. A single-level optimization with the summation of multiple objectives multiplied by some weights w_i is employed in this study. In addition, the objective functions should be greater than some minimum values. The minimum rolling moment ($CR - \beta_{\min}$) for Case 1 and lift coefficient (CL_{\min}) for Case 2 are identified as -0.0004363 per degrees and 1.05, respectively, in correspondence with Yildirim (2021). The conditions, constraints, uncertainties, and design objectives are summarized in Table 4.

3.6.2 Results of IDEM with 5 and 25 POD coefficients

Robust solutions were obtained for the full model, i.e., using 37 design variables for comparison purposes. The number of candidate robust solutions was 1054 out of 5000 design alternatives when all the 37 design variables were used. Among these solutions, the design configuration that gives the minimum objective function value was determined. Similarly, for the case of 5 and 25 POD coefficients, there are 670 and 717 candidate design configurations, respectively. The geometric properties, objective function, and HD-EMI results of the initial and design configurations for both 5 and 25 POD coefficients, and 37 design variables are listed in Table 6. The geometry changes are evaluated based on the geometric parameters given in Figs. 4 and 5. The geometry of each of these configurations for 5 and 25 POD coefficients and 37 design variables are shown in Fig. 4 along with the initial wing geometry for comparison. Moreover, the root and tip airfoil profiles of the configurations are shown in Fig. 5 to evaluate the design differences for 5 and 25 POD coefficients, and 37 design variables.

It is seen from Table 5 that 5 POD and 25 POD coefficients, and 37 design variables lead to different geometric values as well as objective function and HD-EMI values. The taper ratio, in other words, the ratio of the tip chord length to root chord length of the wing is higher than the

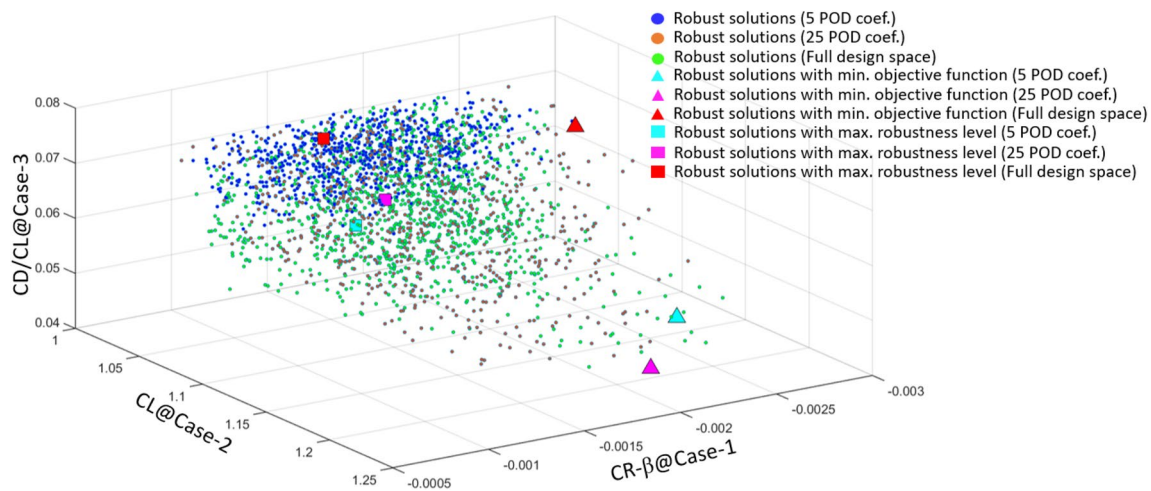


Fig. 6 Robust solutions obtained by IDEM computations. (Color figure online)

initial geometry for all three robust configurations of 25 POD coefficients and 37 design variables while it is only lower for the configuration of 5 POD coefficients. The highest taper ratio is found to be 0.61 for all cases. This is also visible from the top views in Fig. 4a where the robust configurations have smaller root and longer tip chord lengths compared to the initial wing geometry. The aspect ratio results of all robust solutions are higher than that of the initial geometry as seen in Table 5. The higher semi-span length values in Fig. 4a support this observation. Similarly, the dihedral angle for the robust solution of both 5 and 25 POD coefficients is also smaller than the initial configuration as seen in Fig. 4c while the dihedral angle for the robust solution of 37 design variables is higher than the initial configuration as seen in Fig. 4c. The main discrepancy is observed in the sweep angle of the robust solutions which is almost two times the initial geometry as seen in Fig. 4a. Furthermore, the magnitude of twist angle values for all robust solutions is smaller than the initial geometry seen in Fig. 4b.

The tip and root airfoil profiles are also plotted in Fig. 5 for three design configurations obtained by 5 and 25 POD coefficients, 37 design variables, and initial configuration. The root profile thicknesses for all design variables tend to reduce compared to the initial design except for the robust solution of 25 POD coefficients seen in Fig. 5a. The tip profile thickness tends to increase compared to the initial design seen in Fig. 5b except for the robust solution of 5 POD coefficients. There is almost no difference observed in the leading edge radius, maximum camber, and camber location for the root and tip airfoil profiles obtained by 5 POD coefficients and 37 design variables compared to the initial geometry seen in Fig. 5a and b. However, there is a significant discrepancy observed for the root and tip airfoil profiles obtained by 25 POD coefficients seen in Fig. 5a and b.

The objective function results in Table 5 show that all three robust design configurations have lower objective function values than the initial geometry as expected by the minimization objective of the optimization process. In addition, the HD-EMI value indicates how far away a design point is from the boundary determined in correspondence with the constraints and uncertainties. Therefore, the high HD-EMI value is the criterion to identify the robustness level of the design alternatives. If the designer desires to increase the robustness level of the solution alternative, the robust solutions that have higher HD-EMI design alternatives are selected. In that respect, all three design configurations for 37 design variables give higher robustness and lower objective function value compared to the design solutions for both 5 and 25 POD coefficients. This result indicates that more design freedom exists when a higher number of design variables (37 in this study) is used to further minimize the objective function with increased robustness. Nevertheless, according to the results in Table 5 and Figs. 4, and 5, using the POD approach still gives acceptable results compared to the entire design space with 37 design variables.

To further investigate this observation, all robust solutions obtained from the IDEM calculations within the design space are shown in Fig. 6. The blue, orange, and green points show the robust configurations obtained with 5 and 25 POD coefficients, and 37 design variables, respectively. It is seen that the robust solutions obtained with 5 POD coefficients (blue points) are concentrated in a smaller region of the design space, whereas the robust solutions obtained with both 25 POD coefficients (orange points) and 37 design variables (green points) are scattered over a wider region.

The cyan, magenta, and red triangles represent the three robust configurations in Table 5, which have the minimized objective function values with 5 and 25 POD coefficients, and 37 design variables, respectively. It is observed that

Table 7 Geometric properties of robust solutions with maximum robustness level for 5 and 25 dominant POD coefficients, and 37 design variables

Configuration	Taper ratio	Aspect ratio	Dihedral angle (°)	Sweep angle (°)	Twist angle (°)	Objective function	HD-EMI
Initial	0.50	5.91	5.00	5.00	− 1.50	0.546	0.743
5 POD coefficients	0.46	5.89	5.17	5.50	− 1.67	0.530	1.275
25 POD coefficients	0.51	5.36	5.36	6.06	− 2.33	0.441	1.797
37 Design variables	0.41	4.74	6.62	5.04	− 0.66	0.429	1.885

Table 8 MAE (%) results between the estimated values and CFD results

Configuration	$CR - \beta @ Case-1$	$CL @ Case-2$	$CD/CL @ Case-3$
5 POD coefficients-minimum objective function values	0.49	1.50	0.82
5 POD coefficients-maximum robustness level	2.18	2.79	1.39
25 POD coefficients-minimum objective function values	1.02	1.51	0.70
25 POD coefficients-maximum robustness level	5.07	1.08	2.09
37 Original design variables-minimum objective function values	0.86	2.32	7.63
37 Original design variables-maximum robustness level	2.96	1.67	3.18

the results for all scenarios are obtained near the bound of the corresponding design space. This result is attributed to the fact that there is no valid geometry alternative within the design limits given in Table 1, which correspond to the bounds of 5 POD coefficients listed in Table 10, 25 POD coefficients listed in Table 11, and 37 design variables listed in Table 1. Besides, the results for 37 design variables give more minimum objective function values compared to those for 5 and 25 POD coefficients as seen in Table 5. Therefore, it can be said that the increase in the number of the POD coefficients leads to more design freedom, resulting in an improved design in terms of the objective function value.

Furthermore, the cyan, magenta, and red squares in Fig. 6 denote the robust configurations which have the highest robustness level or in other words HD-EMI value. The results of these configurations are listed in Table 6. It is observed from Fig. 6 that the solutions are moving towards the center of the design space with an increasing robustness level. However, the objective function values of these points with higher robustness are not minimized. These results indicate that there is a trade-off between the robustness level and the objective function values.

It is also worth noting that the points with the highest robustness levels for 5 and 25 POD coefficients, and 37 design variables are close to each other (i.e., clustered in the same region) as shown in Fig. 6. The closeness of them indicates that similar objective function values were obtained for the design configurations with the highest robustness level for 5 and 25 POD coefficients, and 37

Table 9 Comparison of computational time required for the design space exploration

Design space	Computational time (h)
5 POD coefficients	74.5
25 POD coefficients	371.2
37 original design variables	565.6

design variables. Then, it can be concluded that the presented IDEM framework can provide appropriate results when only 5 POD coefficients are used, which is decided based on the energy content value in Sect. 3.3. Thus, these results show that the computational effort of the robust shape optimization of the aircraft wing is reduced while still appropriate design configurations are obtained compared to those obtained with the use of a higher number of POD coefficients, decided to be 25 according to RMS results in Sect. 3.3.

To investigate the effect of higher robustness and more minimum objective values on the geometric parameters of the wing, the results given in Tables 5 and 6 are also compared. It is seen from Table 6 that the taper ratios for the robust configurations obtained by 5 POD coefficients and 37 design variables are lower, and the taper ratio obtained by 25 POD coefficients is higher than that of the initial geometry. The aspect ratio values given in Table 6, on the other hand, are smaller for all configurations compared to

those of configurations with the most minimum objective values given in Table 5 and the initial geometry. Besides, the configurations with the highest robustness have greater dihedral angle values given in Table 6 than the values of the configurations with the most minimum objective values except for 37 design variables given in Table 5. On the contrary, the sweep angle values given in Table 6 are not as high as the ones given in Table 5, which indicates that the higher robustness levels are achieved with lower sweep angles. However, lower sweep angles also bring an increase in the objective function values. Similarly, the magnitude of the twist angle values for the configurations which have the highest robustness levels given in Table 6 are also higher except for 37 design variables than the values of those with the most minimum objective values given in Table 5.

The wing geometry and airfoil profiles of three design configurations obtained by 5 and 25 POD coefficients, 37 original design variables, and initial configuration are also shown in Figs. 7 and 8. Compared with the airfoils for the configurations with the most minimum objective values given in Fig. 4, similar behaviors for the maximum thickness, camber and camber location, and leading edge radius are observed except that the root profile thickness for 25 POD coefficients tends to increase with the increase of the robustness level.

3.6.3 Validation of optimized solutions with CFD simulations

CFD simulations were carried out for all the optimized wing design configurations described in Tables 5 and 6. The POD-RBF estimations obtained by the improved IDEM were evaluated by comparing them with the CFD responses which were considered to be the true responses. The calculated mean absolute error (MAE) values for comparison are listed in Table 7.

The results show that the highest MAE result is below 8%, which indicates that the POD-RBF predictions and the true CFD responses are in good agreement for the robust solutions. Specifically, for the design optimization with 5 design variables, the maximum MAE result is 1.50% for the response of CL at Case 2 as seen in Table 7 which means very accurate predictions were obtained by the POD-RBF with 5 design variables. On the other hand, the robust solutions obtained from the design optimization with 37 design variables have larger MAE results compared to those with both 5 and 25 design variables. These results show that using a higher number of design variables reduces the objective function value compared to using 5 modes, but predicts the

results with slightly lower accuracy. The lower accuracy for 37 design variables can be attributed to the complexity of the input–output connections due to the increased number of design variables (i.e., inputs). Nevertheless, the errors are lower than 9% which is enough to conclude that regardless of the number of design variables POD-RBF can produce estimations with acceptable accuracy according to the results for all design variables.

3.6.4 Comparison of required computational cost for optimization

It is mentioned in Sect. 2.6 that the true response of the design alternatives is evaluated by steady-state CFD analyses. Each steady-state CFD analysis for the design space exploration was performed using 200 compute-node processors. The computational cost of database generation is given in Table 8.

It is seen from Table 9 that the design space generation with 5 POD coefficients can essentially reduce the computational time (74.5 h), almost five times compared to that of the database generation with 25 POD coefficients (371.2 h) and almost eight times compared to that of the database generation with 37 original design variables (565.6 h) defined in Sect. 3.2. That means the design space generation with 5 POD coefficients can essentially reduce the computational time that is required for the evaluation of the true response of the design alternatives with CFD analyses. Therefore, the design space constructed with a fewer number of POD coefficients is suitable for the limited computational time and/or resources. However, the results both in Tables 5 and 6 show that there are drawbacks in terms of the objective function values and robustness level with decreasing POD coefficients. Designs with better minimum objective function values and a higher robustness level can be identified with increasing POD coefficients if there is no concern in terms of computational time.

4 Conclusion

In this study, an efficient multi-objective robust shape optimization methodology is presented to be used for an aircraft wing design with a high number of design variables by integrating POD with a design exploration method called IDEM. POD is introduced for two different purposes to the IDEM. The first one is related to the geometry filtration process to reduce the number of design variables required for the optimization framework of IDEM. Initially, 37 design variables

were required to parametrize a wing geometry using Bezier surfaces. The dominant features which identify the wing geometry were evaluated, and the number of design variables was reduced from 37 to 5 based on 99% energy content criterion. In terms of RMSE results, on the other hand, convergence was obtained for 25 POD coefficients. To evaluate the influence of 5 and 25 POD coefficients, the IDEM is implemented for both 5 and 25 coefficients.

The second POD usage field is the POD-based RBF surrogate modeling to enrich design alternatives for the design space generation in IDEM. The prediction capability of the in-house written POD-RBF curve fitting algorithm was found to be in very well agreement with the RBF method presented in the reliable open-source optimization tool DAKOTA. The responses of 5000 unknown discrete design points generated by the LHS technique were estimated using POD-RBF. Model uncertainty due to the turbulence models to be used for the robust optimization process is introduced to the IDEM with the eigenspace perturbation methodology.

Five distinct CFD analyses for three different design conditions (three for eigenvalue perturbation and two for eigenvector perturbation) are performed to obtain the perturbed solutions. The uncertainty bound for the design objectives is computed with the discrepancy between the perturbed and unperturbed solutions.

The robust solutions are acquired by IDEM computations and put in an order starting from the one that gives the most minimum objective function value. The candidate robust design alternatives are selected and compared with the initial wing geometry for the design space with 5 and 25 POD coefficients, and 37 design variables. The results showed that the design space generation with 5 POD coefficients can essentially reduce the computational time, which is required for the evaluation of the true response of the design alternatives with CFD analyses, about five and eight times compared to that of the generation with 25 POD coefficients and 37 original design variables, respectively. However, the robust configurations obtained by 25 POD coefficients and 37 original design variables produced lower objective function and higher HD-EMI values compared to those obtained by 5 POD coefficients. This result is expected because a high number of design variables to represent the same geometry means more freedom of optimization and a high number of points in the POD-RBF to find better solutions. On the other hand, similar objective function value magnitudes were obtained

for the configurations with the highest robustness level with 5 and 25 POD coefficients, and 37 original design variables, which indicates that the energy content that suggests 5 POD coefficients is a suitable criterion to reduce the computational effort and produce configurations with high robustness levels. Furthermore, the comparisons with actual CFD analysis results gave better accuracy when 5 POD coefficients were used compared to the results with 25 POD coefficients, which indicates that more reliable predictions can be made during the optimization process. Therefore, identifying the POD coefficients based on the energy content and constructing the design space with a smaller number of POD coefficients is found to be a suitable approach for the limited computational time and/or resources. More robust and optimized results can be found with increasing POD coefficients. In both cases, it is concluded that the improved IDEM with POD is an effective design exploration tool that can be used in the aerodynamic field to find an optimal design range for the specified performance conditions. Future work includes the consideration of the input uncertainties in the optimization to have a rigorous design evaluation.

Appendix A: design limits of 5 POD coefficients

Design space exploration for the design space constructed using 5 POD coefficients is achieved with the limits given in Table 10.

Table 10 Design limits for the design space constructed by 5 POD coefficients

Design space	Lower bound	Initial wing geometry	Upper bound
POD coefficient-1	− 2.015661	− 0.201566	2.015661
POD coefficient-2	− 1.021244	− 0.928403	1.021244
POD coefficient-3	− 0.773974	− 0.019349	0.773974
POD coefficient-4	− 0.747255	0.106751	0.747255
POD coefficient-5	− 0.308858	0.000515	0.308858

Appendix B: design limits of 25 POD coefficients

Design space exploration for the design space constructed using 25 POD coefficients is achieved with the limits given in Table 11.

Table 11 Design limits for the design space constructed by 25 POD coefficients

Design space	Lower bound	Initial wing geometry	Upper bound
POD coefficient-1	− 2.015661	− 0.201566	2.015661
POD coefficient-2	− 1.021244	− 0.928403	1.021244
POD coefficient-3	− 0.773974	− 0.019349	0.773974
POD coefficient-4	− 0.747255	0.106751	0.747255
POD coefficient-5	− 0.308858	0.000515	0.308858
POD coefficient-6	− 0.185192	0.016836	0.185192
POD coefficient-7	− 0.119841	0.003995	0.119841
POD coefficient-8	− 0.096005	0.0096	0.096005
POD coefficient-9	− 0.097971	0.002177	0.097971
POD coefficient-10	0.080307	− 0.000945	− 0.080307
POD coefficient-11	− 0.04988	0.006235	0.04988
POD coefficient-12	0.041061	− 0.002053	− 0.041061
POD coefficient-13	− 0.018082	0.001808	0.018082
POD coefficient-14	0.028347	− 0.001288	− 0.028347
POD coefficient-15	− 0.021807	0.000661	0.021807
POD coefficient-16	0.014772	− 0.005909	− 0.014772
POD coefficient-17	− 0.020388	0.002039	0.020388
POD coefficient-18	− 0.016324	0.000653	0.016324
POD coefficient-19	− 0.013035	0.001534	0.013035
POD coefficient-20	− 0.012748	0.000283	0.012748
POD coefficient-21	− 0.007595	0.000169	0.007595
POD coefficient-22	− 0.009292	0.000465	0.009292
POD coefficient-23	− 0.005044	0.000126	0.005044
POD coefficient-24	− 0.004892	0.000489	0.004892
POD coefficient-25	− 0.004077	0.000063	0.004077

Appendix C: robust solutions with maximum robustness level for 5 and 25 POD coefficients and 37 design variables

For the first three robust solutions with maximum robustness levels obtained by 5 and 25 POD coefficients and 37 design variables, the wing geometries and the airfoil profiles are given in Figs. 7 and 8, respectively.

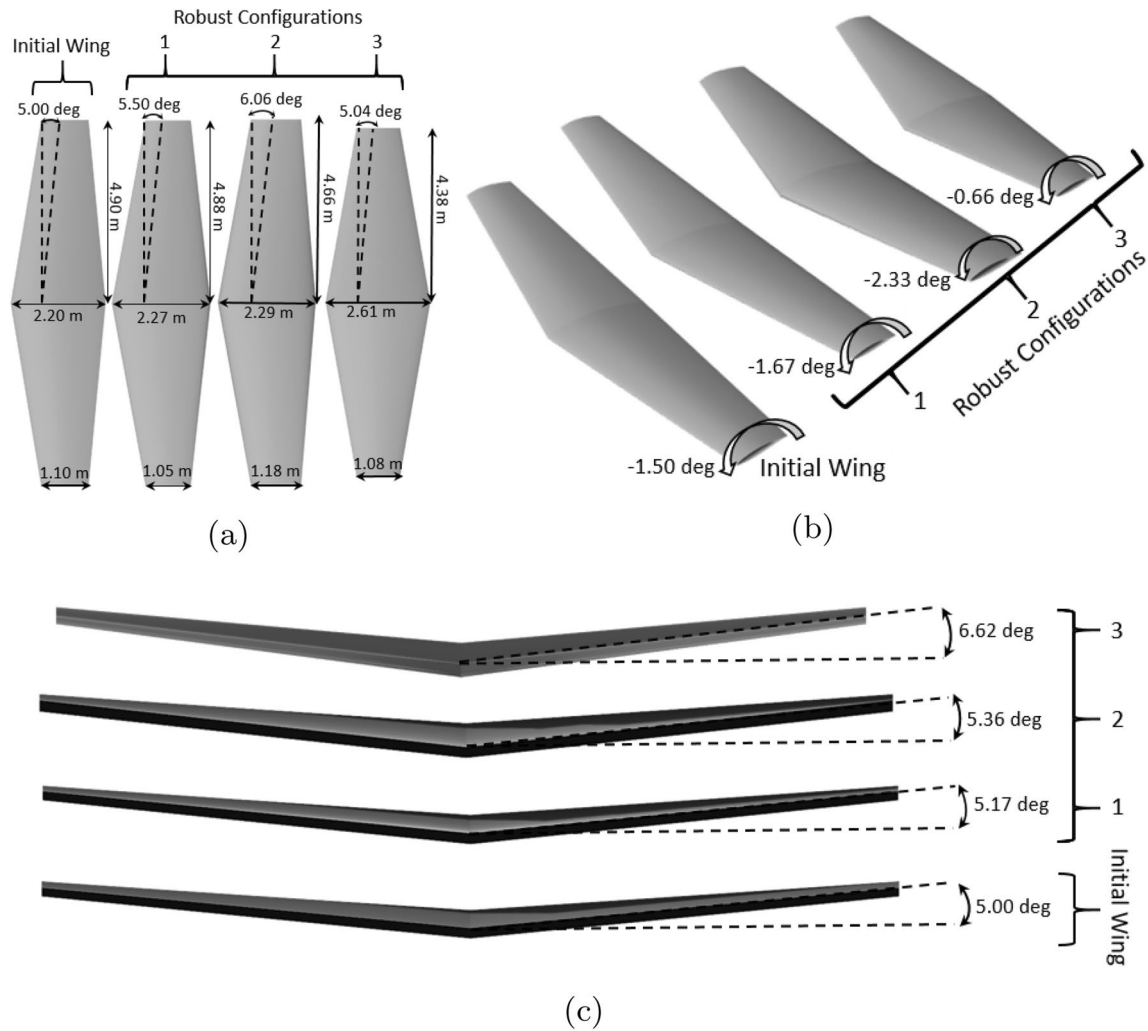


Fig. 7 Robust solutions with maximum robustness level obtained by 5 and 25 POD coefficients and 37 design variables **a** Top view, **b** Isometric view, **c** Front view

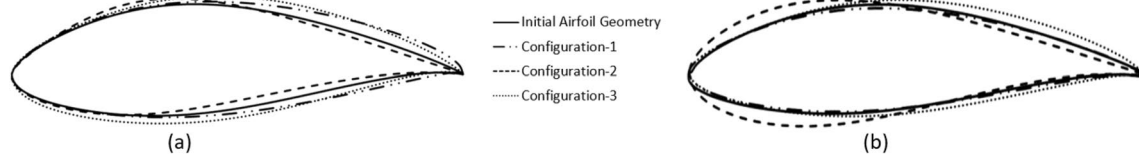


Fig. 8 Robust airfoil profiles with maximum robustness level **a** root and **b** tip airfoil profiles for 5 and 25 POD coefficients, and 37 design variables

Supplementary Information The online version contains supplementary material available at <https://doi.org/10.1007/s00158-023-03557-1>.

Acknowledgements This research did not receive any specific grant from funding agencies in the public, commercial, or not-for-profit sectors.

Data availability The data and material can be made available upon reasonable request.

Code availability An in-house Python script was developed for the POD-RBF surrogate modeling based on the open-source Python code for IDEM, called pyDEM (Kern et al. 2017).

Declarations

Conflict of interest On behalf of all authors, the corresponding author states that there is no conflict of interest.

Replication of results All necessary information to obtain the data to reproduce the results was provided in this paper. The results described in this paper can be replicated by implementing this information. The numerical codes to reproduce the results can also be provided by the corresponding author with a reasonable request.

References

- Afzal A, Kim KY, Seo JW (2017) Effects of Latin hypercube sampling on surrogate modeling and optimization. *Int J Fluid Mach Syst* 10:240–253. <https://doi.org/10.5293/IJFMS.2017.10.3.240>
- Akossou AYJ, Palm R (2013) Impact of data structure on the estimators R-square and adjusted R-square in linear regression. *Int J Math Comput* 20:84–93
- Amrit A, Leifsson L, Koziel S (2018) Multi-fidelity aerodynamic design trade-off exploration using point-by-point Pareto set identification. *Aerosp Sci Technol* 79:399–412. <https://doi.org/10.1016/j.ast.2018.05.023>
- Anderson J (1999) *Aircraft performance and design*, 5th edn. McGraw-Hill, New York, pp 199–319
- Benaissa B, Köppen M, Wahab MA, Khatir S (2017) Application of proper orthogonal decomposition and radial basis functions for crack size estimation using particle swarm optimization. *J Phys Conf Ser* 842:012014. <https://doi.org/10.1088/1742-6596/842/1/012014>
- Bird GD, Gorrell SE, Salmon JL (2021) Dimensionality-reduction-based surrogate models for real-time design space exploration of a jet engine compressor blade. *Aerosp Sci Technol* 118:107077. <https://doi.org/10.1016/j.ast.2021.107077>
- Bons NP, He X, Mader CA, Martins JRRA (2017) Multimodality in aerodynamic wing design optimization. In: 18th AIAA/ISSMO multidisciplinary analysis and optimization conference. <https://doi.org/10.2514/1.J057294>
- Caboni M, Minisci E, Riccardi A (2018) Aerodynamic design optimization of wind turbine airfoils under aleatory and epistemic uncertainty. *J Phys* 1037:042011. <https://doi.org/10.1088/1742-6596/1037/4/042011>
- Cai X, Ladeinde F (2005) A comparison of two POD methods for airfoil design optimization. In: 35th AIAA fluid dynamics conference and exhibit 4912. <https://doi.org/10.2514/6.2005-4912>
- Castonguay P, Nadarajah S (2007) Effect of shape parametrization on aerodynamic shape optimization. In: 45th AIAA aerospace sciences meeting and exhibit. <https://doi.org/10.2514/6.2007-59>
- Choi HJ, Allen JK, Rosen D, McDowell DL, Mistree F (2005) An inductive design exploration method for robust multiscale materials design. *J Mech Des* 130:031402. <https://doi.org/10.1115/1.2829860>
- Choi HJ, Allen JK, Rosen D, McDowell DL, Mistree F (2008) an inductive design exploration method for the integrated design of multi-scale materials and products. In: International design engineering technical conferences and computers and information in engineering conference, vol 4739. pp 859–870. <https://doi.org/10.1115/DETC2005-85335>
- Dalbey K, Eldred MS, Geraci G, Jakeman JD, Maupin KA, Monschke JA, Seidl DT, Swiler LP, Tran A, Menhorn F, Zeng X. (2020) Dakota A Multilevel Parallel Object-Oriented Framework for Design Optimization Parameter Estimation Uncertainty Quantification and Sensitivity Analysis, Technical report. <https://doi.org/10.2172/1630693>
- Deane AE, Kevrekidis IG, Karniadakis GE, Orszag SA (1991) Low-dimensional models for complex geometry flows: application to grooved channels and circular cylinders. *Phys Fluids A* 3(10):2337–2354. <https://doi.org/10.1063/1.857881>
- Du X, He P, Martins JRRA (2021) Rapid airfoil design optimization via neural networks-based parametrization and surrogate modeling. *Aerosp Sci Technol* 113:106–701. <https://doi.org/10.1016/j.ast.2021.106701>
- Meheut M, Dumont A, Carrier G, Peter JE. (2016) Gradient-based optimization of CRM wing-alone and wing-body-tail configurations by RANS adjoint technique. In: 54th AIAA aerospace sciences meeting. <https://doi.org/10.2514/6.2016-1293>
- Economon TD, Palacios F, Copeland SR, Lukaczyk TW, Alonso JJ (2015) SU2: an open-source suite for multiphysics simulation and design. *AIAA J* 54:1–19. <https://doi.org/10.2514/1.J053813>
- Emory M, Pecnik R, Iaccarino G (2011) Modeling structural uncertainties in Reynolds-averaged computations of shock/boundary layer interactions. 49th AIAA aerospace sciences meeting including the new horizons forum and aerospace exposition 479. <https://doi.org/10.2514/6.2011-479>
- Farin G (1993) *Curves and surfaces for computer aided geometric design*, 3rd edn. Elsevier, Amsterdam
- Ferguson J (1964) Multivariable curve interpolation. *J ACM* 11(2):221–228. <https://doi.org/10.1145/321217.321225>
- Fornet M, Rohr K, Stiehl HS (2001) Radial basis functions with compact support for elastic registration of medical images. *Image Vis Comput* 19:87–96. [https://doi.org/10.1016/S0262-8856\(00\)00057-3](https://doi.org/10.1016/S0262-8856(00)00057-3)
- Fusi F, Quaranta G (2020) Assessment of robust optimization for design of rotorcraft airfoils in forward flight. *Aerosp Sci Technol* 107:106–355. <https://doi.org/10.1016/j.ast.2020.106355>
- Hicks R, Henne P (1978) Wing design by numerical optimization. *J Aircr* 15(2):407–412. <https://doi.org/10.2514/3.58379>
- Huntington DE, Lyrantzis CS (1998) Improvements to and limitations of Latin hypercube sampling. *Probab Eng Mech* 13(4):245–253. [https://doi.org/10.1016/S0266-8920\(97\)00013-1](https://doi.org/10.1016/S0266-8920(97)00013-1)
- Iuliano E (2011) Towards a POD-based surrogate model for CFD optimization. In: Proceedings of the ECCOMAS CFD and optimization: conference 49
- Iuliano E (2017) Global optimization of benchmark aerodynamic cases using physics-based surrogate models. *Aerosp Sci Technol* 67:273–286. <https://doi.org/10.1016/j.ast.2017.04.013>
- Iuliano E, Quagliarella D (2013) Aerodynamic shape optimization via non-intrusive POD-based surrogate modelling. *IEEE Congr Evol Comput*. <https://doi.org/10.1109/CEC.2013.6557736>
- Jameson A (1994) Analysis and design of numerical schemes for gas dynamics artificial diffusion, and discrete shock structure. *Int J Comput Fluid Dyn* 5:1–38. <https://doi.org/10.1080/10618569508940734>

- Jang S, Choi HJ, Choi SK, Oh JS (2018) Inductive design exploration method with active learning for complex design problems. *Appl Sci* 8:2418. <https://doi.org/10.3390/app8122418>
- Kennard RW, Stone LA (1969) Computer aided design of experiments. *Technometrics* 11(1):137–148. <https://doi.org/10.2307/1266770>
- Kern PC, Priddy MW, Ellis BD, McDowell DL (2017) pyDEM: a generalized implementation of the inductive design exploration method. *Mater Des* 134:293–300. <https://doi.org/10.1016/j.matdes.2017.08.042>
- Koo D, Zingg DW (2018) Investigation into aerodynamic shape optimization of planar and nonplanar wings. *AIAA J* 56:250–263
- Kulfan B, Bussoletti J (2006) Fundamental parametric geometry representations for aircraft component shapes. In: *AIAA/ISSMO multidisciplinary analysis and optimization conference* 6948. <https://doi.org/10.2514/6.2006-6948>
- Kumar Y, Srivastava SK, Bajpai SK, Kumar N (2012) Development of CAD algorithms for Bezier curves/surfaces independent of operating system. *WSEAS Trans Comput* 11(6):159–169
- Kutkan H (2018) Aerothermodynamic shape optimization using DSMC and POD-RBF methods. MS Thesis, Middle East Technical University
- Li J, Zhang M (2021) Data-based approach for wing shape design optimization. *Aerosp Sci Technol* 112:106–639. <https://doi.org/10.1016/j.ast.2021.106639>
- Lim HD, Wei XF, Zang B, Vevek US, Mariani R, New TH, Cui YD (2020) Short time proper orthogonal decomposition of time-resolved Schlieren images for transient jet screech characterization. *Aerosp Sci Technol* 107:106–276. <https://doi.org/10.1016/j.ast.2020.106276>
- Marler RT, Arora JS (2004) Survey of multi-objective optimization methods for engineering. *Struct Multidisc Optim* 26:369–395. <https://doi.org/10.1007/s00158-003-0368-6>
- Menter PR (1994) Two-equation Eddy-viscosity turbulence models for engineering applications. *AIAA J* 32:1598–1605. <https://doi.org/10.2514/3.12149>
- Mishra AA, Mukhopadhyaya J, Iaccarino G, Alonso J (2018) An uncertainty estimation module for turbulence model predictions in SU2. *AIAA J* 57:1066–1077. <https://doi.org/10.2514/1.J057187>
- Nagarajan KK, Cordier L, Airiau C, Kourta A. (2009) POD based reduced order modelling of a compressible forced cavity flow. In: *CFM 2009 - 19ème Congrès français de mécanique*, Marseille, France. <https://hal.science/hal-03390749>
- Newman AJ (1996) Model reduction via the Karhunen-Loeve expansion part I: exposition. <http://hdl.handle.net/1903/5751>
- Rao JR, Roy N (1988) Fuzzy set theoretic approach of assigning weights to objectives in multicriteria decision making. *Int J Syst Sci* 20:1381–1386. <https://doi.org/10.1080/00207728908910222>
- Raul V, Leifsson L (2021) Surrogate-based aerodynamic shape optimization for delaying airfoil dynamic stall using Kriging regression and infill criteria. *Aerosp Sci Technol* 111:106–555. <https://doi.org/10.1016/j.ast.2021.106555>
- Ren Z, Thelen AS, Amrit A, Du X, Leifsson L, Tesfahunegn YA, Koziel S (2016) Application of multifidelity optimization techniques to benchmark aerodynamic design problems. In: *54th AIAA aerospace sciences meeting*
- Rogers CA, Kassab AJ, Divo A, Ostrowski Z, Bialecki A (2012) An inverse POD-RBF network approach to parameter estimation in mechanics. *Inverse Probl Sci Eng* 20:749–767. <https://doi.org/10.1080/17415977.2012.693080>
- Romani L, Rossini M, Schenone D (2019) Edge detection methods based on RBF interpolation. *J Comput Appl Math* 349:532–547. <https://doi.org/10.1016/j.cam.2018.08.006>
- Schulze D (2005) Far field boundary conditions based on characteristic and bicharacteristic theory applied to transonic flows. In: *14th international conference on numerical methods in fluid dynamics*, vol 453. pp 211–215. <https://doi.org/10.1007/3-540-59280-6124>
- Sirovich L (1997) Chaotic dynamics of coherent structures. *Physica* 37:126–145. [https://doi.org/10.1016/0167-2789\(89\)90123-1](https://doi.org/10.1016/0167-2789(89)90123-1)
- Sobieczky H (1998) Parametric airfoils and wings. *Recent Dev Aerodyn Des Methodol*. <https://doi.org/10.1007/978-3-322-89952-14>
- Sripawadkul V, Padulo M, Guenov M (2010) A comparison of airfoil shape parametrization techniques for early design optimization. In: *AIAA/ISSMO multidisciplinary analysis and optimization conference*. <https://doi.org/10.2514/6.2010-9050>
- Wendland H (1995) Piecewise polynomial, positive definite and compactly supported radial functions of minimal degree. *Adv Comput Math* 4:389–396. <https://doi.org/10.1007/BF02123482>
- Wen-Long W, Hua L, Sha P (2011) Performance comparison and analysis of different schemes, and limiters. *Int J Phys Math Sci* 5(7):974–979. <https://doi.org/10.5281/zenodo.1081197>
- Xiao H, Wu JL, Wang JX, Sun R, Roy CJ (2016) Quantifying and reducing model-form uncertainties in Reynolds-averaged Navier–Stokes simulations: a data-driven, physics-informed Bayesian approach. *J Comput Phys* 324:115–136. <https://doi.org/10.1016/j.jcp.2016.07.038>
- Xin C, Li L, Teng L, Zhenjiang Y (2015) A reduced order aerothermodynamic modeling framework for hypersonic vehicles based on surrogate and POD. *Chin J Aeronaut* 28:1328–1342. <https://doi.org/10.1016/j.cja.2015.06.024>
- Yang F, Chen Z (2021) Multi-objective aerodynamic optimization using active multi-output Gaussian process and mesh deformation method. *J Aerosp Eng*. <https://doi.org/10.1177/095441002110021>
- Ye Y, Wang X, Zhang X (2021) Cascade ensemble-RBF-based optimization algorithm for aero-engine transient control schedule design optimization. *Aerosp Sci Technol* 115:106–779. <https://doi.org/10.1016/j.ast.2021.106779>
- Yildirim BY (2021) Aerodynamic shape optimization of a wing using 3D flow solutions with SU2 and response surface methodology. MS Thesis, Middle East Technical University
- Yu Y, Lyu Z, Xu Z, Martins JRRR (2018) On the influence of optimization algorithm and initial design on wing aerodynamic shape optimization. *Aerosp Sci Technol* 75:183–199. <https://doi.org/10.1016/j.ast.2018.01.016>
- Zhang J, Tang H, Chen M (2021) Robust design of an adaptive cycle engine performance under component performance uncertainty. *Aerosp Sci Technol*. <https://doi.org/10.1016/j.ast.2021.106704>
- Zhou LL, Jiu LJ, Jun Z, Kuan L, Ni YM (2020) Aerodynamic shape optimization by continually moving ROM. *Aerosp Sci Technol* 99:105–729. <https://doi.org/10.1016/j.ast.2020.105729>
- Zhu Y, Ju Y, Zhang C (2020) Proper orthogonal decomposition assisted inverse design optimisation method for the compressor cascade airfoil. *Aerosp Sci Technol* 105:105–955. <https://doi.org/10.1016/j.ast.2020.105955>

Publisher's Note Springer Nature remains neutral with regard to jurisdictional claims in published maps and institutional affiliations.

Springer Nature or its licensor (e.g. a society or other partner) holds exclusive rights to this article under a publishing agreement with the author(s) or other rightsholder(s); author self-archiving of the accepted manuscript version of this article is solely governed by the terms of such publishing agreement and applicable law.